Soft Matter

PAPER

View Article Online
View Journal | View Issue

Check for updates

Cite this: *Soft Matter*, 2026, 22, 1739

# Lipstick structure revealed by multimodal strain- and time-dependent rheology

Marie Gautier,[ab] Theany To,[a] Anne-Sophie Botte,[b] Jules Dupire,[b] Tanguy Rouxel *[a] and Franck Artzner *[a]

Since their earliest developments, lipsticks have been heterogeneous wax/oil-based cosmetics enriched with pigments and nacres. Originally made from basic constituents, formulations have substantially evolved, now incorporating a variety of advanced components such as polymers, silicones, and fillers, as consumers have become more and more demanding about product performance. This evolution has made the mechanisms underlying macroscopic properties of lipsticks increasingly complex. Understanding their mechanical behavior under stress has therefore become important for formulation design and product performance optimization. In this study, the elastic properties as well as linear and non-linear viscoelastic properties of three grades of commercially available lipsticks are explored through compression experiments and rheological shear and oscillatory measurements. A model based on the Kohlrausch–Williams–Watts (KWW) function is proposed to describe the creep behavior in the linear viscoelastic regime. At large deformations, lipsticks exhibited intracycle strain-stiffening and shear-thinning nonlinearities leading to structural breakdown, as revealed by Lissajous–Bowditch plots and Fourier analysis, while microcracking eventually occurred under compression. This work shows that, although the studied lipsticks exhibit distinct macroscopic properties reflecting different material textures, they all seem to follow the same constitutive law within the linear range. Two relaxation regimes are identified, with a crossover at about 10 seconds separating short- and long-timescale responses. Moreover, the identification of a continuous spectrum of relaxation mechanisms by strain- and time-dependent rheological experiments points to an intertwined architecture that likely underlies the mechanical stability of lipsticks.

Received 10th October 2025,
Accepted 18th January 2026

DOI: 10.1039/d5sm01032b

rsc.li/soft-matter-journal

## Introduction

Lipsticks are iconic makeup products that reflect significant cultural and societal changes over time.[1,2] The earliest evidence of lipstick use can be traced back to the Bronze Age, with the discovery of a cylindrical vial containing a mixture of vegetal waxes and mineral pigments.[3] Today, lipsticks have become a strategic and key product in the beauty industry, with significant sales worldwide.[4] Psychologists have even highlighted the ''lipstick index'', linking lipstick sales to economic recessions.[5,6] Particularly in the luxury industry, customers expect flawless, aesthetically pleasing lipsticks. With changing market trends, sensory properties and product finish on lips have become critical aspects, leading to frequent evolutions in formulation. Originally made from basic constituents such as oils, waxes, butters and pigments, modern formulae have been enriched with multiple ingredients including polymers, silicones, and fillers, to meet the ever-growing performance demands of consumers. Here, we distinguish silicones from polymers as they fulfil different functional roles in lipsticks: polymers are chosen for their long-lasting effects as well as their thickening properties, whereas silicones, often oligomers in cosmetics, are associated with texture and spreadability. As a result, modern lipsticks are usually composed of more than thirty ingredients.[7] The desired sensory finish of a lipstick can impact other macroscopic properties. For instance, when consumers seek soft lipsticks that melt upon application, the product's resistance to breakage may be compromised due to a decreased firmness. Additionally, current market trends driven by the ''Clean Beauty'' movement call for the substitution of synthetic raw materials with natural alternatives. This shift adds further complexity to lipstick formulation, as synthetic waxes have been used for decades and offer unique mechanical properties and stability.[8–10]

Multiple parameters must be considered during formulation to balance sensory qualities and overall product stability, including mechanical and thermal requirements. While several studies have focused on the mechanisms underlying their sensory properties[4,11,12] and thermal stability,[10,13–15] the

---

[a] *Univ Rennes, CNRS, IPR (Institut de Physique de Rennes) – UMR 6251, F-35000 Rennes, France. E-mail: tanguy.rouxel@univ-rennes.fr, franck.artzner@univ-rennes.fr*

[b] *CHANEL Parfums Beauté, IR&D, 93500 Pantin, France*

mechanical properties of lipsticks remain poorly understood. To establish links between microstructure and mechanical behavior and to understand crystallization kinetics, Wang *et al.* studied simplified lipstick systems made of wax and oil mixtures.[16] Moreover, in other industrial sectors such as food science or oil science, fat crystallization and lipid-based materials properties are well-established areas of research and present similarities with lipstick systems.[17–22] Nevertheless, to our knowledge, none of the studies have investigated the mechanical behavior and mechanical stability of full-formula lipsticks at room temperature, even though lipsticks must withstand a variety of stresses during application and are expected to perform reliably under mechanical loading.[23,24]

Among complex systems, intertwined architectures, arising from the interplay of different ingredients, often lead to enhanced mechanical properties, particularly in terms of stiffness and ductility.[25–30] Such architectures are especially relevant when considering the structure of complex composite materials like lipsticks, which comprise multiple structuring ingredients such as waxes and polymers, whose interactions are still not fully understood. Waxes have traditionally been central to lipstick formulations due to their ability to crystallize into three-dimensional networks of variable rigidity, contributing to the product's mechanical integrity. Moreover, it is well-established that mixing waxes of different types can result in either synergistic or antagonistic interactions, which may strengthen or weaken the mechanical performance of the crystalline network.[16,31] The increasing use of polymers over the past three decades has enabled the development of textures better suited to market trends and consumer expectations.[7] Polymers form networks of entangled chains capable of sliding over each other under stress, thus contributing to the mechanical behavior of the product.[32] This intertwined architecture of waxes and polymers is therefore considered as a potential underlying factor contributing to both the mechanical stability and functional performance of lipsticks, including sensory properties and effective deposition on the lips.

By investigating the mechanical behavior of commercialized lipsticks, the present work aims to deepen our understanding of their structure and behavior under in-use conditions.

## Materials and methods

### Materials

Experiments were conducted on samples taken from three distinct commercially available lipsticks, each formulated with different ingredients and in varying proportions of lipidic composition, and referred to as LS-1, LS-2 and LS-3. The benchmark lipsticks were selected based on variations in texture rendering, stick properties, and formulation, with the aim of better understanding the relationships between the composition, microstructure, and rheological properties. LS-1, with the smallest percentage of waxes in formula, is a soft and glossy product, while LS-3, with the largest wax content, appears matte and hard. LS-2 is an intermediate product regarding wax content and sensorial properties, displaying more traditional lipstick characteristics with intermediate firmness and smoothness. Furthermore, LS-1 and LS-2 contain only waxes and oils, while LS-3 contains waxes, oils, and butters. Besides fatty components, the lipsticks also contain a significant proportion of additives such as pigments, nacres, oil-soluble emollients, fillers, silicones and polymers, which can affect wax crystallization.[33,34] It is noteworthy that LS-1 has the largest polymer content in its formulation, while LS-3 has the lowest. LS-2 falls in between. The main characteristics of the studied lipsticks, including formulation and melting profiles, are summarized in Table 1. Lipstick textures are shown on Fig. 1.

### Methods

**LC-PolScope imaging.** The LC-PolScope is a birefringence imaging technique based on circularly polarized light microscopy, allowing the birefringence to be represented as a vector, with a magnitude (measured in retardance) and an orientation angle. Observations were conducted using an inverted polarized light microscope (IX70, Olympus, Japan) equipped with a ×20 microscope objective (LCPlanFI, Olympus, Japan) and a CCD camera with a 12-bit, 1024 × 1392 resolution sensor (Oosight, Hamilton Thorne Inc., USA). Thanks to an additional liquid crystal universal compensator and a circularly polarized light analyser (Oosight, Hamilton Thorne Inc., USA), the LC-PolScope allows visualization of both the orientation and magnitude of each birefringent structure of the sample by combining a greyscale retardance image, illustrating the magnitude of birefringence, and a colored orientation image, illustrating the orientation of these birefringent elements at angles between 0° and 180° relative to the horizontal axis of the image.[35,36] In this technique, the occurrence of colored regions is related to birefringence effects stemming either from crystallized phases or from the alignment of polymer chains for example. Samples were collected from lipsticks and pressed into a thin film between two microscope glasses. This imaging

Table 1 Main composition and texture of the three studied lipsticks

| Sample | Fat composition: Mass fraction of wax | Fat composition: Mass fraction of oils | Fat composition: Mass fraction of butter | Mass fraction of polymers | Aspect and texture | Melting range: Onset | Melting range: Endset | Melting range: Peak |
|---|---|---|---|---|---|---|---|---|
| LS-1 | <13% | <55% | 0% | >13% | Soft and glossy | 13.5 °C | 81.6 °C | 74.9 °C |
| LS-2 | 13–17% | >55% | 0% | <5% | Classic (traditional lipstick texture) | 21.3 °C | 86.6 °C | 75.4 °C |
| LS-3 | >17% | >55% | <5% | <5% | Hard and matte | 21.3 °C | 87.6 °C | 66.4 °C |

Fig. 1 Lipstick texture rendering after application on synthetic skin of LS-1 (soft and glossy), LS-2 (classic), and LS-3 (hard and matte), from left to right.

technique was used to characterize wax crystal size and morphology, as well as the spatial distribution of the crystals.

In order to quantitatively analyze the crystal distribution in the micrographs, we used the open-source ImageJ software.[37] To enhance particle identification and improve the counting process, the colored micrographs were split into eight separate images based on hue thresholds, with each image covering a 32-value range in the 8-bit hue channel (0–255). In terms of angle, this segmentation corresponds to a separation of birefringence orientations into 22.5° increments. A 2-pixel mean filter was applied to reduce noise, and the particles were counted for each hue-segmented image. The total number of particles in a micrograph was then determined by summing the counts from all hue segments.

**Oscillatory shear rheology.** A TA Instruments DHR-2 stress-controlled rheometer, equipped with a fixed Peltier plate allowing for temperature control, and a software collecting measured data (TRIOS 5.1, TA Instruments, USA), was used to carry out all oscillatory rheological measurements. A 12-mm diameter mobile upper plate geometry was chosen to conduct thermal sweeps, amplitude sweeps and frequency sweeps. To avoid slippage of the samples during isothermal measurements, both upper and lower plates were covered with a P600 SiC abrasive paper, secured with a rigid and temperature resistant glue (up to 70 °C). Before measurements, lipsticks were stored in a proofer set at 20 °C for at least 12 hours. Samples were cut directly from the lipsticks into thin slices of approximately 1.5 mm in height by means of a steel wire and deposited on the Peltier stage. The mobile geometry was lowered until meeting the sample and establishing the desired gap of 1 mm. The excess lipstick paste was then removed with a spatula. A cover was placed over the sample in order to minimize heat dissipation. For all isothermal measurements, the temperature of the Peltier stage was maintained at 20 °C. Amplitude sweeps were performed at fixed frequencies of $\omega$ = 0.1 Hz and $\omega$ = 1 Hz across a strain amplitude range of $10^{-5} < \gamma_0 < 1$. Frequency sweeps were performed at a fixed strain amplitude of $\gamma_0 = 10^{-4}$ across a frequency range of $10^{-2}$ Hz $< \omega < 10^{2}$ Hz. Thermal sweeps were performed by cooling the samples from the molten state at 100 °C to the room temperature (20 °C) at a rate of 5 °C min$^{-1}$, applying a fixed strain amplitude of $\gamma_0 = 10^{-3}$ and fixed frequency of $\omega$ = 1 Hz. In order to analyze the rheological response of the lipsticks as a function of their cooling rate, samples were cooled on the rheometer from 90 °C to 20 °C and after one hour of stabilization at 20 °C, amplitude sweeps were performed.

In this study, a sinusoidal strain (angular distortion), $\gamma(t) = \gamma_0 \sin(\omega t)$, was imposed to explore the behavior from the linear viscoelastic (LVE) range, in small amplitude oscillatory shear (SAOS), to the non-linear range in large amplitude oscillatory shear (LAOS).

*Small amplitude oscillatory shear (SAOS).* In the LVE zone, the shear stress response to a sinusoidal strain also takes a sinusoidal signal $\tau(t) = \tau_0 \sin(\omega t + \delta)$, where $\tau_0$ is the shear stress response amplitude and $\delta$ is the phase shift (also referred to as the loss angle). The storage modulus $G'$ (real part of $G^*(t)$) and the loss modulus $G''$ (imaginary part of $G^*(t)$), as well as the loss factor $\tan(\delta) = G''/G'$, can be determined from the complex shear modulus $G^*(t) = \dfrac{\tau(t)}{\gamma(t)}$. The LVE zone is characterized by a plateau in the storage modulus $G'$ at small strain amplitudes and displays the intrinsic rheological properties of the samples.[38]

*Large amplitude oscillatory shear (LAOS).* Exiting the LVE zone is associated with a decrease in $G'$ and $G''$, indicating that the material begins to deform.[39] In this non-linear zone, the stress response to a sinusoidal strain signal is no longer sinusoidal.[40] In the frequency domain, this implies that, in addition to the fundamental frequency, higher harmonics begin to affect the signal. In this case, the shear stress response takes the form $\tau(t) = \sum_{n=1}^{\infty} \tau_n \sin(n\omega t + \delta_n)$, where $n$ represents higher-order harmonics, $\tau_n$ and $\delta_n$ are the corresponding amplitudes and phase angles of the shear stress response, respectively, and $\omega$ is the pulsation of the applied oscillatory strain ($\omega = 2\pi f$, where $f$ is the frequency). In this study, we focus on the first and third harmonics of the stress response.

Several techniques were developed to analyze and interpret the non-sinusoidal shear stress response. For qualitative interpretation, Lissajous–Bowditch curves are often useful to catch the effect of frequency and amplitude on the non-linear response. Strain–stress curves characterize elastic contribution to the non-linear response while strain rate-stress curves reveal the viscous contribution.[41] The shape of these Lissajous–Bowditch curves allows for a visual interpretation of the non-linear behavior in terms of shear-thinning or shear-thickening, as well as strain-softening or strain-stiffening.[41,42] For a quantitative interpretation, the most common technique is the Fourier Transform (FT) rheology, allowing to obtain the Chebyshev coefficients (for detailed methodology, see SI 1).[43–47]

Nevertheless, the Chebyshev decomposition raises difficulty of physical interpretation due to potential singularities inherent in its mathematical definition. To better capture non-linearities, a strain-stiffening ratio $S$ (eqn (1)) and a shear-thickening ratio $T$ (eqn (2)), based on the Chebyshev coefficients, were further proposed by Ewoldt *et al.*[41] These ratios can also be determined from the Lissajous–Bowditch curves and interpreted in terms of non-linear behavior. A positive $S$ value indicates strain-stiffening, whereas a negative $S$ value signifies strain-softening. Similarly, a positive $T$ value denotes shear-thickening, while a negative $T$ value indicates shear-thinning.

$$S = \frac{4e_3 + \ldots}{e_1 + e_3 + \ldots} = \frac{G'_{\mathrm{L}} - G'_{\mathrm{M}}}{G'_{\mathrm{L}}} \tag{1}$$

and

$$T = \frac{4\nu_3 + \ldots}{\nu_1 + \nu_3 + \ldots} = \frac{\eta'_{\mathrm{L}} - \eta'_{\mathrm{M}}}{\eta'_{\mathrm{L}}} \tag{2}$$

where $e_1$ and $e_3$ are the first order and third order elastic Chebyshev coefficients, respectively (SI 1). $G'_{\mathrm{M}}$ is the minimum-strain modulus or tangent modulus at minimum strain and $G'_{\mathrm{L}}$ is the large-strain modulus or secant modulus at the maximum strain. $\nu_1$ and $\nu_3$ are the first order and third order viscous Chebyshev coefficients, respectively. $\eta'_{\mathrm{M}}$ is the local viscosity at the minimum shear rate or tangent modulus at minimum shear rate and $\eta'_{\mathrm{L}}$ is the local viscosity at the maximum shear rate or secant modulus at maximum ear rate, both measured at a specific spatial point of the oscillation cycle.[11]

*Creep and recovery.* Creep and recovery measurements were performed by the same stress-controlled rheometer and parallel plates geometry used for oscillatory rheological measurements. A constant shear stress was applied to cylindrical samples (1 mm high, 12 mm diameter) directly cut from lipsticks. For the same reasons discussed in the context of oscillatory rheology, both plates were covered with P600 sandpaper. During the creep and recovery tests, a shear stress of 250 Pa was abruptly applied on the sample for 15 minutes and then suddenly removed. The small stress level of 250 Pa was chosen to remain below the maximum shear stress supported by all samples, allowing their properties to be probed without altering the structure (Table 2). A recovery time of 45 minutes was observed in order to guarantee that most of the recoverable strain could be relaxed. The strain response was collected using the TRIOS 5.1 software (TA Instruments, USA) provided with the rheometer.

*Rheological modeling.* The aim of the creep and recovery measurements is to characterize the time-dependent rheological behavior. When performing creep tests, we measure the compliance $J(t)$ of the material, which refers to its ability to deform under the applied load: $J(t) = \gamma(t)/\tau(t)$, where $\gamma(t)$ is the strain (dimensionless) and $\tau(t)$ (Pa) is the shear stress. The compliance curve can be modelled by a combination of elementary cells such as springs, dashpots, friction pads (for threshold stresses), *etc.*, thanks to the linear viscoelastic constitutive equations.[48–50] During recovery, the stress is released, and compliance cannot be directly computed. We therefore denote the strain-based quantity measured during recovery as $J_{\mathrm{R}}(t)$. In this study, the Burgers model, consisting of a Maxwell model (one spring and one dashpot in series), in series with a Kelvin-Voigt model (one spring and one dashpot in parallel) was first considered. The Burgers model is commonly used to describe the stress–response of viscoelastic materials, as it effectively captures instantaneous elasticity, delayed elasticity, and viscous deformation. In more complex systems such as lipsticks, a single Kelvin-Voigt model may be insufficient to account for the extended duration over which the delayed strain occurs. To better capture the material response, $N$ additional Kelvin-Voigt elements can be incorporated in series within the Burgers model.[51] We thus obtain the generalized Burgers model (GBM), corresponding to the following constitutive equations (eqn (3) and (4)):

$$J(t) = \frac{1}{G_0} + \sum_{i=1}^{N} \frac{1}{G_i}\left(1 - \mathrm{e}^{-\frac{t}{\tau_i}}\right) + \frac{t}{\eta_0} \quad \text{during creep (for } t \le t_{\mathrm{c}}) \tag{3}$$

$$J_{\mathrm{R}}(t) = \frac{1}{G_0} + \sum_{i=1}^{N} \frac{1}{G_i}\left(1 - \mathrm{e}^{-\frac{(t-t_{\mathrm{c}})}{\tau_i}}\right) + \frac{(t-t_{\mathrm{c}})}{\eta_0} \quad \text{after creep (for } t > t_{\mathrm{c}}) \tag{4}$$

where $t$ is the experimental duration, $t_{\mathrm{c}}$ is the duration of the creep step, $G_0$ (Pa) is the instantaneous shear elasticity modulus, $\eta_0$ (Pa s) is the shear viscosity coefficient and $\tau_i = \eta_i/G_i$, where $i = [0; N]$, are the characteristic time constants related to the delayed elastic response.

However, lipsticks are highly heterogeneous, disordered systems and their relaxation behaviour cannot be captured well by discrete relaxation times. A more realistic description is obtained by using a continuous distribution of relaxation times, which can be represented with a stretched-exponential creep model based on the Kohlrausch–Williams–Watts (KWW) function[52] (eqn (5) and (6), Fig. 2):

$$J(t) = \frac{1}{G_0} + \frac{1}{G_1}\left(1 - \mathrm{e}^{-\left(\frac{t}{\tau}\right)^{\beta}}\right) + \frac{t}{\eta_0} \quad \text{during creep (for } t \le t_{\mathrm{c}}) \tag{5}$$

Table 2 Storage modulus ($G'$), loss modulus ($G''$), loss factor $\tan(\delta)$, $\gamma_{\mathrm{lim}}$, $\gamma_{\mathrm{crossover}}$ and stress at onset of the nonlinear regime $\tau_{\mathrm{lim}}$ measured during strain amplitude sweep oscillatory rheological tests conducted at 1 Hz and 20 °C

| | $G'$ (MPa) | $G''$ (MPa) | $\tan(\delta)$ | $100 \times \gamma_{\mathrm{lim}}$ | $100 \times \gamma_{\mathrm{crossover}}$ | $\tau_{\mathrm{lim}}$ (Pa) |
|---|---|---|---|---|---|---|
| LS-1 | 1.15 ± 0.28 | 0.35 ± 0.05 | 0.32 ± 0.04 | 0.03 ± 0.01 | 4.6 ± 1.4 | 426 ± 75 |
| LS-2 | 1.80 ± 0.17 | 0.60 ± 0.02 | 0.32 ± 0.02 | 0.03 ± 0.01 | 11.3 ± 1.6 | 633 ± 13 |
| LS-3 | 2.19 ± 0.11 | 0.54 ± 0.01 | 0.24 ± 0.01 | 0.04 ± 0.01 | 28.9 ± 0.1 | 833 ± 26 |

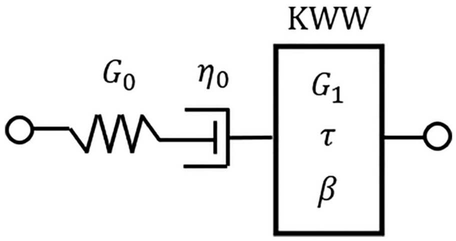

Fig. 2 Schematic representation of the rheological KWW Model. $G_0$ and $G_1$ are the shear elastic moduli. $\eta_0$ is the shear viscosity coefficient. $\tau$ is the characteristic relaxation time and $\beta$ is the KWW-exponent.

$$J_{\mathrm{R}}(t) = \frac{1}{G_0} + \frac{1}{G_1}\left(1 - \mathrm{e}^{-\left(\frac{(t-t_\mathrm{c})}{\tau}\right)^{\beta}}\right) + \frac{(t - t_\mathrm{c})}{\eta_0} \qquad (6)$$

after creep (for $t > t_\mathrm{c}$)

where $\beta$ is an empirical exponent ($0 < \beta < 1$) representing the width of the relaxation spectrum and capturing relaxation heterogeneity, and $\tau$ is the characteristic relaxation time.

The estimation of the parameters in the models was performed by fitting the creep curves using the least squares method. The model's reliability was assessed using the root sum squares (RSS) method (see SI 4).

*Uniaxial compression tests.* Uniaxial compression tests were performed at a constant displacement rate of 10 μm s$^{-1}$ using a stress-controlled Discovery HR-2 rheometer (TA Instruments, USA) set in axial force mode. The samples were cylindrical with dimensions of 15 mm in height and 12 mm in diameter. The samples were placed between a large fixed lower plate and a mobile 40-mm diameter upper plate. Experiments were carried out at ambient temperature (20 °C). Cylindrical specimens were cut directly from the commercial lipsticks with a steel wire and a 3D-printed custom mold to ensure parallelism of the cylinder faces and stored in a 20 °C proofer for at least 12 hours. Before starting the experiment, a normal force of 1 ± 0.1 N was applied for 2 s and then relieved, in order to establish a good contact between the upper plate and the specimen.

Additional tests were performed at a 5000 μm s$^{-1}$ compression rate to favor a pure elastic behavior allowing for the determination of Young's modulus ($E$). All tests were performed thrice to ensure reproducibility.

## Results

### Microstructure

**A cooling-rate dependent microstructure.** The microstructures of the three lipstick samples, obtained under three different cooling rates from 90 °C to 20 °C and analyzed one day after cooling using LC-PolScope imaging, are shown in Fig. 3. For a given cooling rate of 10 °C min$^{-1}$, significant differences in the microstructure show up depending on the lipstick grade. While all lipsticks mainly exhibit needle-like crystals, LS-3 also contains spherical objects. These spherulites, originating from bead-shaped mattifying agents in the formula, are not wax material but may affect the 3D wax network by strengthening its structure or, conversely, weakening it. The crystal size is similar for LS-2 and LS-3, while slightly larger for LS-1. Moreover, LS-1 exhibits larger birefringent areas, possibly due to its high polymer content.

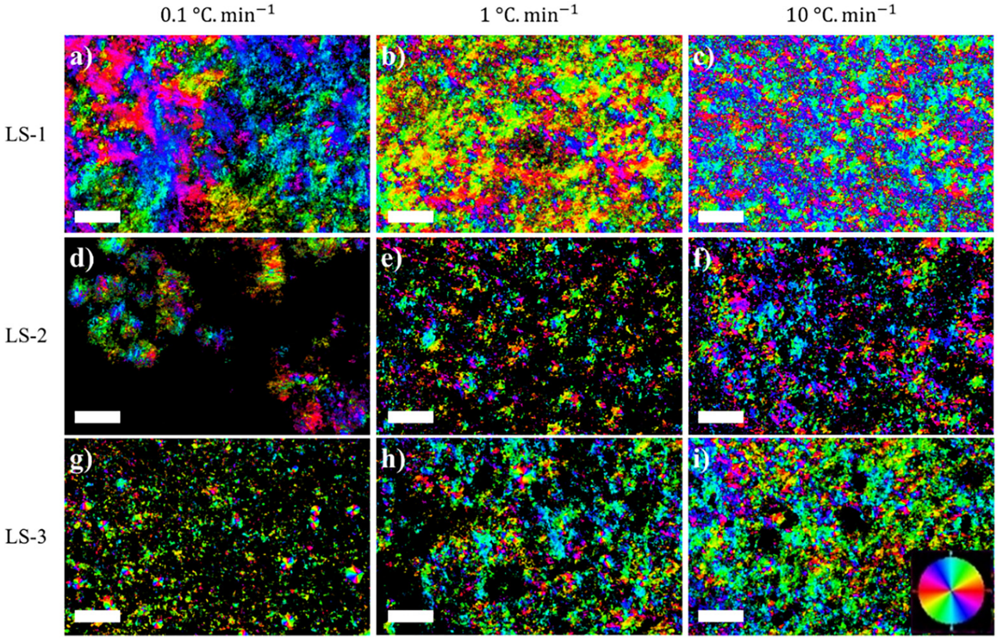

Fig. 3 LC-PolScope imaging of LS-1 (a)–(c), LS-2 (d)–(f), and LS-3 (g)–(i) at 20 °C after submitting the samples to cooling ramps at a rate of 0.1 °C min$^{-1}$, 1 °C min$^{-1}$ and 10 °C min$^{-1}$ (from left to right). The white bar is 50 μm. The colored orientation scale shown at the bottom right (Fig. 3i) applies to all micrographs and indicates the crystal direction relative to the axis of the polarizing filters.[35]

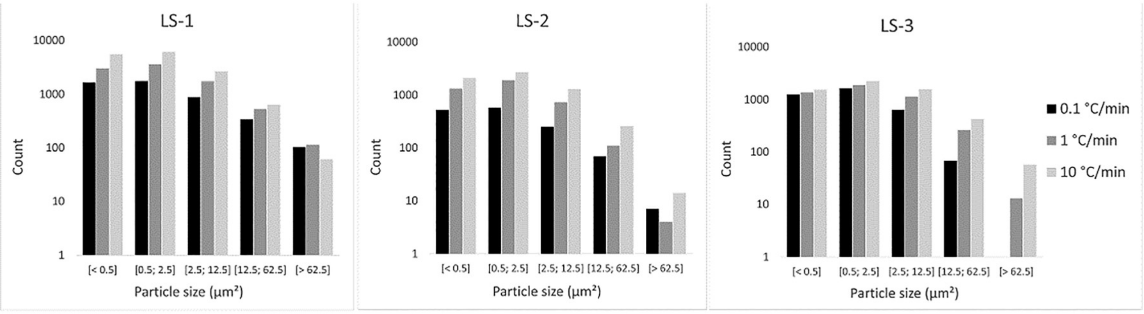

Fig. 4 Particle size distribution histograms (number of particles in each size bin, in log scale) of LS-1, LS-2 and LS-3 measured after cooling at three different rates: 0.1 °C min$^{-1}$, 1 °C min$^{-1}$ and 10 °C min$^{-1}$.

In order to better understand the crystallization kinetics, we observed the evolution of the lipstick microstructure for three different cooling rates: 0.1 °C min$^{-1}$, 1 °C min$^{-1}$ and 10 °C min$^{-1}$. When cooling at a 0.1 °C min$^{-1}$ rate, the crystals in LS-1 and LS-2 are large and sparse. Particularly for LS-2, large and disconnected clusters of needle-crystals are observed, with similar or nearly identical orientations, embedded in a predominantly amorphous oily phase. As the cooling rate increases to 1 °C min$^{-1}$ and 10 °C min$^{-1}$, the number of small crystals increases with crystal connectivity, resulting in a finer microstructure.

These observations are further supported by the quantitative analysis displayed in Fig. 4 where the log-scale particle size distribution histograms reveal a sharp increase in the number of smaller particles with higher cooling rates. In contrast, the number of large particles is less dependent on the cooling rate. For instance, in LS-1, the smaller particle ($<0.5$ µm$^2$) count rises from 1656 at 0.1 °C min$^{-1}$ to 5498 at 10 °C min$^{-1}$, while the large particle ($>62.5$ µm$^2$) count decreases from 104 to 61.

**Microstructure and its influence on rheological behavior.** Wang *et al.* showed that the hardness of wax–oil mixtures depends on microstructural characteristics.[16] Similarly, Patel *et al.* found that organogels displaying loose entanglements of large crystals can sustain smaller stress than those composed of smaller crystals densely packed into larger aggregates.[53] In order to understand the impact of the microstructure on the rheological properties of our lipsticks, we analyzed the rheological behavior (oscillatory amplitude tests) of the LS-2 samples subjected to three different cooling rates, in regard to their corresponding micrographs (Fig. 5). In agreement with the literature, a strong link between microstructure and viscoelastic moduli was observed.

In the case of a rapid cooling, the microstructure consists of small crystals closely packed in small aggregates and the sample exhibits a larger storage modulus. Conversely, with slow cooling where large crystals form into sparse aggregates, both storage and loss modulus significantly decrease.

These observations confirm that a dense structure, composed of interconnected small crystals, results in enhanced rheological properties characterized by a larger stiffness.[54–56] The same relationship between microstructure and rheological properties was observed for the other grades LS-1 and LS-3 (see SI 2). These findings suggest that a stiffer material can be obtained by a rapid cooling. However, it is important to avoid an excessively rapid cooling, as this could lead to an unstable crystal network or crystals that are too small to effectively interconnect.[57] Moreover, although not measured here, the crystallite fraction is a key parameter that strongly impacts mechanical properties.

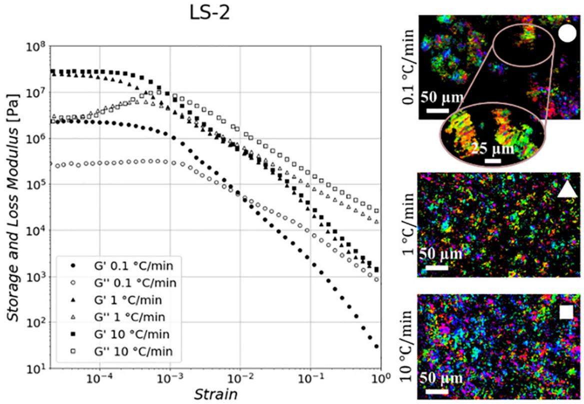

Fig. 5 Rheological oscillatory strain amplitude sweeps at 20 °C of LS-2 samples subjected to three cooling rates 0.1 °C min$^{-1}$ (circles), 1 °C min$^{-1}$ (triangles) and 10 °C min$^{-1}$ (squares) and corresponding LC-PolScope micrographs.

## Rheological behavior under shear stress

### Rheological profiling

*Small amplitude oscillatory shear (SAOS) rheology.* Thermal sweeps were performed from 100 °C to 20 °C to evaluate how the structure of the materials evolves with temperature (Fig. 6).

For all samples, we observe a sharp increase in both storage and loss moduli around their melting temperature. As expected, the structure is viscoelastic with an elastic dominance at lower temperatures, with $\tan(\delta) < 1$. At 20 °C, the loss factor is 0.65 for LS-1, 0.58 for LS-2, and 0.43 for LS-3. Below their melting point, the crystallized waxes and butters start forming a three-dimensional network. Interestingly, we also observe an elastic-dominated viscoelastic behavior at high temperatures, when the fat crystals are melted. This residual elasticity in the molten lipstick is not due to the fat-based ingredients, but instead to other components in the formula such as polymeric networks.[58,59]

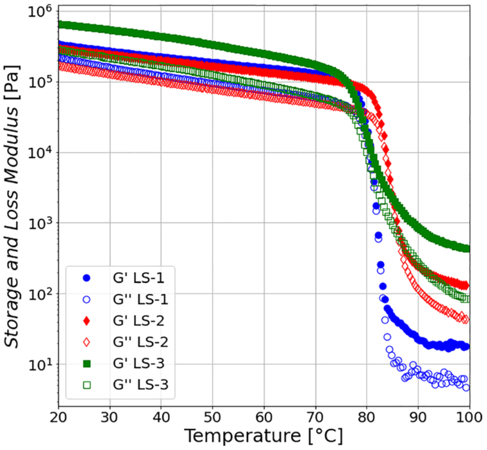

**Fig. 6** Thermal sweeps from 100 °C to 20 °C at 1 Hz and $\gamma = 10^{-4}$ of reference lipsticks LS-1 (blue circles), LS-2 (red diamonds), and LS-3 (green squares), representing the evolution of the storage modulus $G'$ (filled markers) and the loss modulus $G''$ (empty markers) as a function of temperature during oscillatory rheological measurements.

The storage and loss moduli, $G'$ and $G''$, obtained by means of oscillatory strain amplitude sweeps at 1 Hz over a $10^{-5} < \gamma_0 < 1$ amplitude range are shown in Fig. 7 for the different materials. In the LVE zone, that is the regime where the rheological properties don't depend on the strain amplitude (for $\gamma < \gamma_{\text{lim}}$), the material remains unaltered, undergoing elastic reversible deformation.

The $G'$, the $G''$, the $\tan(\delta)$, and the $\gamma_{\text{lim}}$ values for each lipstick in the LVE regime are given in Table 2. LS-3 shows a larger $G'$ value, indicating greater rigidity, whereas LS-1 exhibits the lowest modulus, with LS-2 falling in between. LS-1 and LS-2 exhibit much larger damping ($\tan(\delta) \approx 0.32$) as compared to LS-3 ($\tan(\delta) \approx 0.24$). For all samples, $G'$ is larger than $G''$ over the LVE zone. The length of the LVE zone provides further information into strain amplitude tolerability before plastic deformation occurs.

As $\gamma > \gamma_{\text{lim}}$, both $G'$ and $G''$ decrease with an increase of $\gamma$ and a crossover point ($\gamma_{\text{crossover}}$) where $G' = G''$ shows up. Beyond $\gamma_{\text{crossover}}$, $G'$ is smaller than $G''$ and decreases more rapidly. This evolution reflects a loss of strength in the structure of the material, which is associated with a decrease in shear resistance ($G'$). The easy shear deformation induces internal friction, which is characterized by the $G''$ value. $\gamma_{\text{crossover}}$ values are displayed in Table 2.

Frequency sweeps were conducted at a small strain amplitude of $\gamma = 10^{-4}$, chosen within the LVE zone, to investigate the frequency dependence of the studied lipsticks (Fig. 8). $G'$ was always greater than $G''$ in the measured frequency range. As frequency increases, we observe a rise in the storage modulus $G'$ for all lipsticks. Beyond 0.1 Hz, the $G'$ curves follow a weak power-law, with exponents being close for all lipstick grades: 0.16 for LS-1, 0.14 for LS-2 and 0.11 for LS-3.

Such small slopes are indicative of a gel-like network, where elasticity dominates and the material shows only weak frequency dependence.[60] In parallel, the loss modulus $G''$ curves exhibit a plateau at low frequencies, followed by a steady increase. At very low frequencies, below 0.01 Hz for LS-1 and even lower for the other lipsticks, the materials exhibit terminal flow, indicating the onset of viscous relaxation processes.[60]

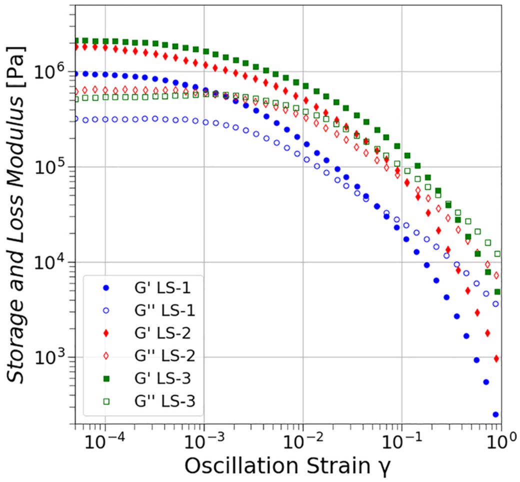

**Fig. 7** Strain amplitude sweeps at 1 Hz of reference lipsticks LS-1 (blue circles), LS-2 (red diamonds), and LS-3 (green squares), representing the evolution of the storage modulus $G'$ (filled markers) and the loss modulus $G''$ (empty markers) as a function of strain amplitude during oscillatory rheological measurements.

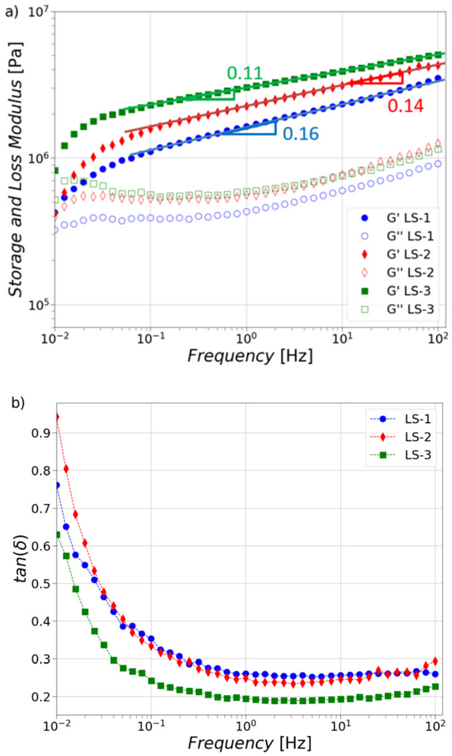

**Fig. 8** Frequency sweeps at $\gamma = 10^{-4}$ of reference lipsticks LS-1 (blue circles), LS-2 (red diamonds), and LS-3 (green squares), representing the evolution of the storage modulus $G'$ (filled markers) and the loss modulus $G''$ (empty markers) (a), and the evolution of the loss factor $\tan(\delta)$ (b), as a function of frequency during oscillatory rheological measurements.

The loss factor, tan($\delta$), decreases sharply with increasing frequency up to 0.1 Hz, reaching a near-zero plateau (Fig. 8b), reflecting reduced damping. Above 0.1 Hz, the material behaves almost like a solid, as deformation occurs too quickly for structural rearrangements, with elastic contributions dominating. Below 0.1 Hz, slower deformation allows relaxation and flow. This classical viscoelastic profile highlights the interplay of multiple structural components and the transition between viscous- and elastic-dominated regimes, with 0.1 Hz ($\approx$10 s) marking a characteristic cutoff.

As explained in the methods section, frequency sweep experiments involve increasing frequency while maintaining a constant strain amplitude. In other terms, this results in a progressively larger mean oscillation strain rate. In our experiment, the oscillation strain rate varies from $\sim 10^{-6}\ \mathrm{s}^{-1}$ at low frequencies to $\sim 10^{-1}\ \mathrm{s}^{-1}$ at high frequencies. Thus, it is consistent to observe that as the strain rate increases, the elastic component becomes predominant. This frequency-dependent behavior is consistent across all three lipstick grades, with LS-3 still exhibiting the greatest rigidity and the smallest damping across the frequency range, while LS-1 shows the smallest rigidity and the greatest damping. Moreover, we emphasize that the studied lipstick samples leave the linear viscoelastic region at very small strain amplitudes. A study involving larger strain amplitudes is required to better understand the evolution of rheological behavior as strain increases.

*Large amplitude oscillatory shear (LAOS) rheology.* Lissajous–Bowditch (L–B) curves for varying strain amplitudes and frequencies provides qualitative information on the LAOS behavior of the lipsticks, in the non-linear viscoelastic (NLVE) zone.[41] Fig. 9 displays the L–B curves for each lipstick, depicting both elastic (stress *vs.* strain) and viscous (stress *vs.* shear rate) contributions.

Similar changes of the curve shape are observed for all lipstick grades. At low strain amplitudes, within the LVE zone, the curves are elliptical. However, as the strain amplitude increases and as the material enters the NLVE zone, the curves become progressively more distorted. These intracycle deformations are typical viscoelastic non-linearities and illustrate intracycle strain-stiffening and shear-thinning behaviors.[11] Moreover, the L–B curves appear disconnected when increasing the strain amplitude, reflecting the onset of irreversible deformation. We observe no significant dependence on frequency.

To perform a quantitative analysis of the LAOS stress response, we convert the temporal signal into a Fourier space and examine the contribution of additional harmonics in a spectral representation (see SI 3).

Fig. 10 displays the evolution of the third harmonic magnitude in the stress response depending on the strain amplitude of our three lipstick materials, normalized against the fundamental's magnitude. At low strains, the third harmonic contribution is negligible. As the material enters the NLVE zone, we observe a progressive increase in its magnitude. The evolution of the third harmonic is similar for LS-1 and LS-2: the curves show a steep initial rise that tapers off as strain increases. Particularly, LS-1 exhibits a noticeable decrease at larger strain. Moreover, LS-3 stands out by displaying a linear evolution, indicating a different non-linear response compared to the other lipsticks.

We chose to perform the *S* and *T* ratios analysis on LS-1 and LS-3, representing the softest and the stiffest materials, respectively. *S* and *T* ratios were calculated at $\gamma_1 = 0.1 \times 10^{-2}$, $\gamma_2 = 1 \times 10^{-2}$, $\gamma_3 = 4 \times 10^{-2}$ and $\gamma_4 = 10 \times 10^{-2}$. (Eqn (1) and (2)).

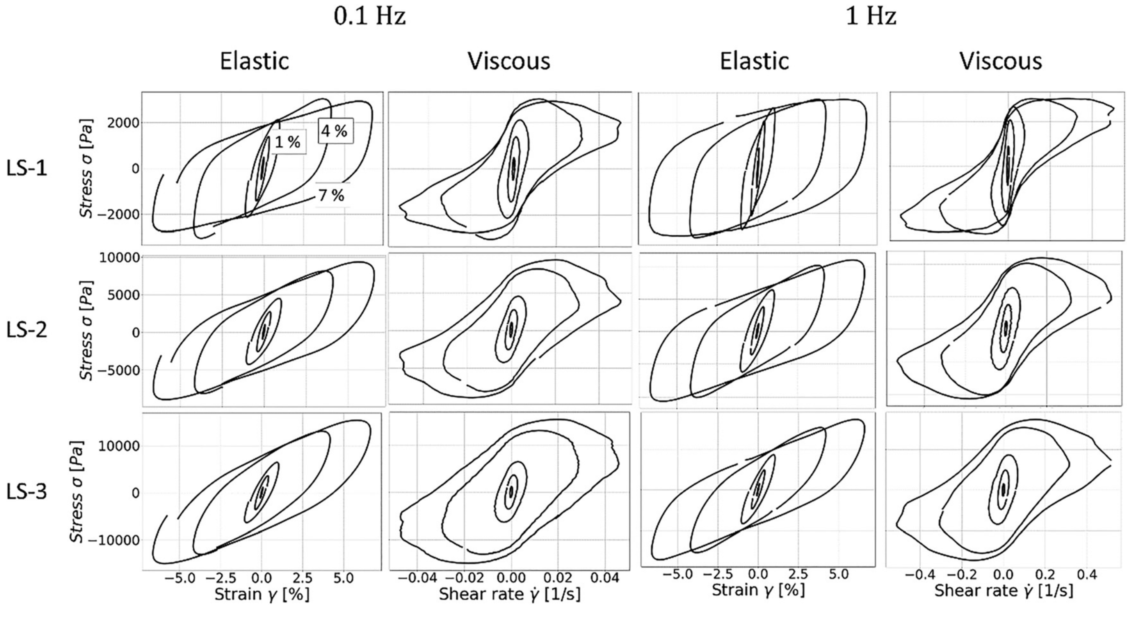

Fig. 9 Elastic (stress *vs.* strain) and viscous (stress *vs.* shear rate) Lissajous–Bowditch curves of the reference lipsticks LS-1, LS-2, and LS-3, for two frequencies 0.1 Hz and 1 Hz and five strain amplitudes $0.1 \times 10^{-2}$, $0.5 \times 10^{-2}$, $1 \times 10^{-2}$, $4 \times 10^{-2}$ and $7 \times 10^{-2}$. Wider Lissajous–Bowditch curves correspond to larger strain amplitudes.

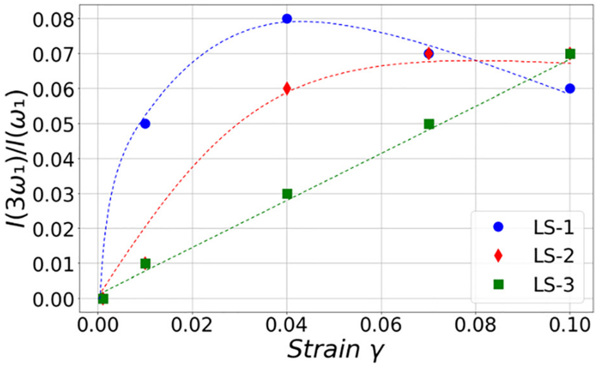

Fig. 10 Normalized magnitude of the third harmonic contribution to the stress response signal in Fourier space normalized by the magnitude of the fundamental, for LS-1 (blue circles), LS-2 (red diamonds), and LS-3 (green squares). Dashed lines serve as guidelines.

At $0.1 \times 10^{-2}$, still within the LVE zone for all lipsticks, both ratios are close to zero. As strain increases, $S$ values increase, indicating intracycle strain-stiffening, while $T$ values decrease, indicating intracycle shear-thinning (Fig. 11).

Particularly, the softer material shows a more pronounced $S$-ratio evolution and a slightly lower one for the $T$-ratio, which reflects stronger strain-stiffening and lower shear-thinning effects. LS-3, which is the stiffer material, seems to exhibit a greater intracycle viscous contribution to non-linearities, whereas the softer one (LS-1) demonstrates a higher intracycle elastic contribution to non-linearities.

LAOS rheology provided interesting insights into the structural breakdown mechanisms occurring in the materials under shear stress, helping to better understand the microstructure of the lipsticks. We note that these structural breakdown mechanisms differ between lipstick grades, reflecting variations in their relaxation behavior and stress responses, which will be further examined in the discussion section. Moreover, the non-linear behaviors observed across all lipstick grades, namely strain-stiffening and shear-thinning, are clearly tied to the microstructure of the materials, a link that will also be examined in more detail later.[38]

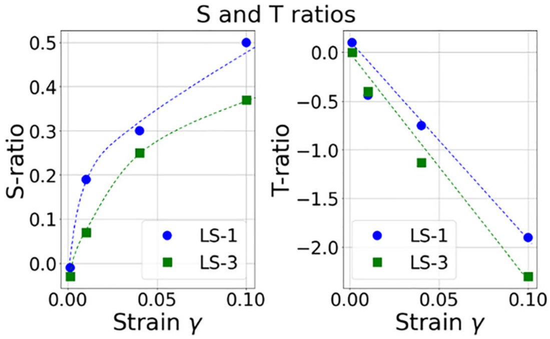

Fig. 11 Evolution of the strain-stiffening ratio ($S$-ratio) and shear-thickening ratio ($T$-ratio) as a function of strain amplitude during amplitude sweep oscillatory rheological measurements at 1 Hz and 20 °C. Data points for LS-1 are represented by blue circles, and LS-3 by green squares. Dashed lines serve as guidelines.

### Creep behavior

*Shear creep experiments.* The creep curves for the three lipstick grades under a mean shear stress of 250 Pa are shown in Fig. 12. The curves exhibit the same three stages, namely (i) the instantaneous elastic deformation, (ii) the delayed elastic deformation and (iii) the viscous deformation. The creep deformation of LS-3 is the smallest, with a maximum strain of $0.08 \times 10^{-2}$, whereas LS-1 showed the largest deformation, reaching up to $0.32 \times 10^{-2}$, that is four times larger. Besides, LS-3 fully recovers from creep deformation after unloading at 900 s, while LS-1 and LS-2 show irreversible strain at the end of the recovery phase.

To quantify sample recovery, we calculate the ratio of instantaneous recovered strain in the total strain $R_{\gamma_{\mathrm{ir}}}$ and the ratio of residual strain in the total strain $R_{\gamma_{\mathrm{ur}}}$:

$$R_{\gamma_{\mathrm{ir}}} = \frac{\gamma_{\mathrm{ir}}}{\gamma_{\max}} \quad \text{and} \quad R_{\gamma_{\mathrm{ur}}} = \frac{\gamma_{\mathrm{ur}}}{\gamma_{\max}}$$

where $\gamma_{\mathrm{ir}}$ is the instantaneous recovered strain, representing the strain that recovers almost instantly once the stress is removed; $\gamma_{\mathrm{ur}}$ is the residual strain at the end of the recovery process, or the irreversible deformation arising from the partial collapse of the waxy network; $\gamma_{\max}$ is the maximum strain reached by the sample at the end of creep. Detailed values of recovering parameters are displayed in Table 3.

Quantitatively speaking, we notice that the proportion of instantaneous recovered strain is particularly large for LS-3. It is smaller for the two other reference lipsticks. Regarding residual strain after the recovery phase, LS-3 achieves full recovery whereas LS-1 and LS-2 retain a higher proportion of residual strain after recovery.

*Creep and recovery modeling.* The experimental creep and recovery compliances $J(t)$ and $J_{\mathrm{R}}(t)$, extracted from the creep and recovery experiments, were used to fit the KWW creep model (eqn (5) and (6)). Since the compliance curves exhibited instantaneous elasticity, delayed elasticity, and viscous flow, we first considered a simple Burgers model with a single Kelvin-Voigt element, but it failed to capture the initial response to loading.

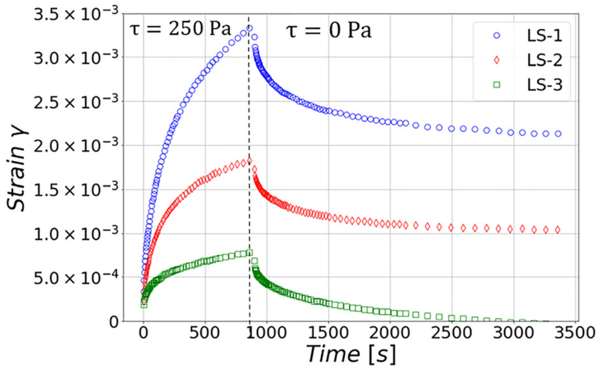

Fig. 12 Overlay of strain curves during shear creep experiments under a torque of 85 μN m corresponding to a mean shear stress of 250 Pa during 900 s and subsequent recovery at 20 °C for LS-1 (blue circles), LS-2 (red diamonds), and LS-3 (green squares).

**Table 3** Recovering quantities extracted from the experimental creep and recovery measurements

| | LS-1 | LS-2 | LS-3 |
|---|---|---|---|
| $\gamma_{\text{ir}}$ | $0.2 \times 10^{-3}$ | $0.1 \times 10^{-3}$ | $0.1 \times 10^{-3}$ |
| $\gamma_{\text{ur}}$ | $2.1 \times 10^{-3}$ | $1.0 \times 10^{-3}$ | 0. |
| $\gamma_{\text{max}}$ | $3.4 \times 10^{-3}$ | $1.8 \times 10^{-3}$ | $0.8 \times 10^{-3}$ |
| $R_{\gamma_{\text{ir}}}$ | 0.06 | 0.08 | 0.18 |
| $R_{\gamma_{\text{ur}}}$ | 0.63 | 0.57 | 0 |

**Table 4** Detailed parameters determined by fitting experimental creep and recovery data to the KWW creep model. Elastic moduli $G_0$ and $G_1$, viscous coefficient $\eta_0$, and relaxation time $\tau$, are expressed in MPa, MPa s, and s, respectively. $\beta$ is dimensionless

| | LS-1 | | LS-2 | | LS-3 | |
|---|---|---|---|---|---|---|
| | Creep | Recovery | Creep | Recovery | Creep | Recovery |
| $G_0$ (MPa) | 1.2 | 55 | 2.1 | 54 | 2.4 | 75 |
| $\eta_0$ (MPa s) | 497 | $\infty$ | 2049 | $\infty$ | 2228 | $\infty$ |
| $G_1$ (MPa) | 0.08 | 0.23 | 0.14 | 0.37 | 0.34 | 0.29 |
| $\tau$ (s) | 258 | 423. | 223 | 373 | 306 | 1217 |
| $\beta$ | 0.62 | 0.57 | 0.58 | 0.58 | 0.42 | 0.52 |

Adding a second Kelvin-Voigt element significantly improved the fit, yet the model remained too limited to describe the heterogeneous relaxation of lipsticks, which occurs over a wide range of timescales. We therefore turned to a KWW-based model, which represents relaxation as a continuous spectrum rather than discrete modes. This approach provided a better description of the compliance curves and resulted in significantly smaller residuals compared to the previous Burgers models (see SI 4). The fitted model is represented by solid lines in Fig. 13, while the experimental data are shown with empty markers. All compliance curves follow a similar trend, regardless of the material.

Fitting the KWW model to our data allows us to extract the materials' elastic moduli $G_0$ and $G_1$, the viscous coefficient $\eta_0$, the characteristic relaxation time $\tau$ and the $\beta$ exponent. The detailed fitting quantities are displayed in Table 4. We then compare these parameters across the different lipstick grades.

It is worth noting that the order of magnitude of the shear rate during the creep experiments is very small, on the order of $10^{-5}$ s$^{-1}$. This very low deformation rate indicates that the material is being probed within the linear regime and allows relaxation processes to occur.

During the creep stage, LS-3 exhibits a larger instantaneous elastic modulus $G_0$, while LS-2 shows a slightly smaller value. LS-1 demonstrates the smallest elastic modulus among the samples. Regarding the viscous coefficient $\eta_0$, it is significantly smaller for LS-1 and increases progressively for LS-2 and LS-3, respectively.

Moreover, the characteristic relaxation time $\tau$, associated with the delayed elastic response, ranges from $\sim$250 s (LS-1 and LS-2) to $\sim$300 s (LS-3), in agreement with LS-1 and LS-2 being the most ductile materials and LS-3 the most brittle. The $\beta$ exponent ranges from $\sim$0.6 (LS-1 and LS-2) to $\sim$0.4 (LS-3), suggesting multiple relaxation mechanisms occurring over a large temporal range and illustrating the heterogeneity of the system. In particular, LS-3 exhibits the broader distribution of relaxation times during creep.

During the recovery stage, the predicted model parameters differ from those obtained during the creep stage. The $G_0$ parameter significantly increases for all our samples. This evolution could be attributed to structural rearrangement, such as crystal alignment, consistently with the strain-stiffening behavior we observed in the LAOS analysis. However, this phenomenon may also be linked to creep effects affecting the measured parameter, as indicated by several reports in the field of nano-indentation on viscoelastic soft materials.[61–63] The stress release may also occur more rapidly than the creep loading.

The viscous coefficient $\eta_0$ also increases significantly during the recovery stage, becoming nearly infinite as the applied stress is removed, indicating that viscous flow no longer occurs. During creep, the applied shear stress reduces the viscosity due to pronounced shear-thinning behavior observed in the LAOS analysis, whereas in recovery, the absence of stress allows the material to respond essentially elastically.

The characteristic relaxation time $\tau$ also exhibits an increase for all samples, indicating longer relaxation mechanisms during recovery. For the LS-1 and LS-2 grades, this time increase is associated with a rise in $G_1$. In contrast, the LS-3 grade shows a subtle decrease of the elastic modulus $G_1$, suggesting a slight weakening of the structure. Interestingly, LS-3 is the only material showing a narrower relaxation-time distribution after creep, reflected by the increase in the $\beta$-value. This indicates a higher degree of structural order after creep.

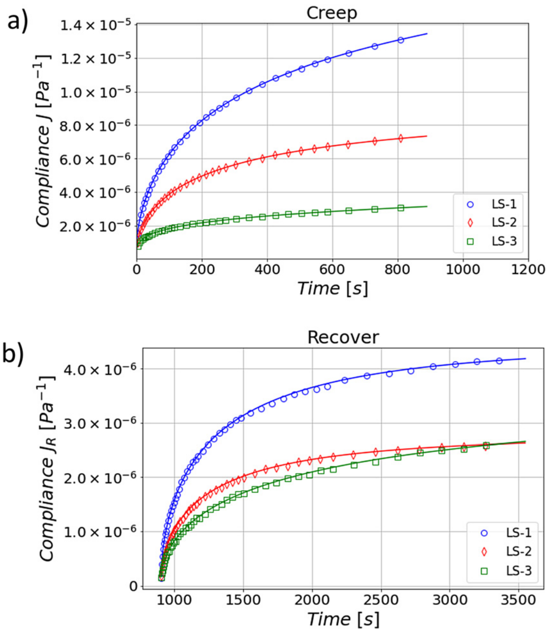

Fig. 13 Creep compliance curves under 250 Pa (a) and recovery compliance curves (b) with corresponding model determined with the KWW creep model. Experimental data are shown with empty markers, while solid lines represent model predictions.

Our observations suggest that the KWW creep model is suitable to model our three reference lipsticks and may serve as a fundamental tool for predicting the viscoelastic behavior of lipsticks under small stress (Fig. 13). In order to validate the relevance of our model, the predicted parameters were correlated with experimental SAOS rheological data (Tables 2 and 4). A comparison of the viscoelastic moduli $G'$ and $G''$ obtained in SAOS with the estimated creep instantaneous elastic modulus $G_0$ reveals a consistent order of magnitude across all values. Notably, LS-1 exhibits the smallest moduli in both the experimental data and model predictions, whereas LS-3 displays the largest moduli.

**Mechanical response under compression.** The maximum stress $\sigma_{\max}$ and corresponding strain $\varepsilon_{\max}$ before failure, as well as the yield stress $R_e$ (also known as the elastic limit), measured at a displacement rate of $\dot{\varepsilon} = 6.7 \times 10^{-4}$ s$^{-1}$, were determined from the stress–strain curves displayed in Fig. 14a. Additionally, the stress–strain curves at a larger displacement rate of $\dot{\varepsilon} = 0.33$ s$^{-1}$ shown in Fig. 14b allowed to obtain the corresponding Young's modulus by minimizing the viscous response of the materials. All the parameters are reported in Table 5.

Among the three studied lipstick grades, LS-3 displays the largest Young's modulus associated with the smallest maximum deformation before failure. LS-1 has the smallest Young's modulus, associated with a large deformation and a relatively low stress before failure. These measurements corroborate the sensory characteristics of the lipsticks, as LS-1 is a soft product while LS-3 is a harder one. Likewise, LS-2, displaying an intermediate stick texture, shows corresponding intermediate values in its stress response. In the compression experiments, the materials are probed in the non-linear regime. This may explain why the maximum stresses of LS-2 and LS-3 overlap, even though LS-3 has been found stronger when probed in the linear regime.

The stress–strain curves (Fig. 14) exhibit three stages, namely (i) the elastic loading until the yield stress ($R_e$) occurs, (ii) a softening range where the stress drops to about $\frac{1}{4}\sigma_{\max}$, and (iii) a "plateau" where $\sigma$ remains constant or slowly increases. The slope in the first stage varies from ~2 MPa (LS-1) to ~9 MPa (LS-3).

Table 5 Mechanical properties of the lipsticks averaged over three independent measurements: the maximum stress ($\sigma_{\max}$), the yield stress or elastic limit ($R_e$) and the strain corresponding to the $\sigma_{\max}$ ($\varepsilon_{\max}$) measured at a compression rate of 10 μm s$^{-1}$. Young's modulus $E$ at a compression rate of 5000 μm s$^{-1}$ to limit the viscoelastic contribution

| | 10 μm s$^{-1}$ | | | 5000 μm s$^{-1}$ |
|---|---|---|---|---|
| | $\sigma_{\max}$ (kPa) | $R_e$ (kPa) | $\varepsilon_{\max}$ (%) | $E$ (MPa) |
| LS-1 | 110 ± 6 | 107 ± 6 | 5.9 ± 0.2 | 7.5 ± 0.8 |
| LS-2 | 170 ± 3 | 144 ± 4 | 5.5 ± 0.1 | 14.3 ± 1.5 |
| LS-3 | 167 ± 3 | 153 ± 7 | 3.4 ± 0.3 | 15.9 ± 2.8 |

The maximum stress can be viewed as a threshold stress to initiate the activation of shear bands, which are further responsible for the softening observed in the secondary stage. The deformation localization in the region near the upper or lower plate, especially for the LS-1 and LS-2 grades, as well as the relatively soft nature of these grades, induces a rapid decrease of the stress beyond the $\sigma_{\max}$ threshold. As shear bands extend through the sample, large pieces of material detach, with a close to 45° angle to the loading axis (Fig. 15a and b).

The deformation is much more uniform in the case of LS-3 grade. This latter material can sustain a relatively large stress or a smaller strain range than the other grades thanks to a larger elastic contribution allowing for a more uniform deformation. The compressive loading ultimately results in the formation of axial cracks (Fig. 15c) as in a brittle material such as a piece of chalk. The observations in Fig. 15, and in particular the shear banding and the microcracking behavior, call for further investigations. Videos of the compression tests are provided in the SI.

Furthermore, we note a significant increase in the slope of the elastic stage with a larger displacement rate (Fig. 14). As we mentioned before, this evolution is likely linked to the viscous component of lipsticks, which are viscoelastic materials.

In such materials, the mechanical response is time-dependent and results from an interplay between the elastic

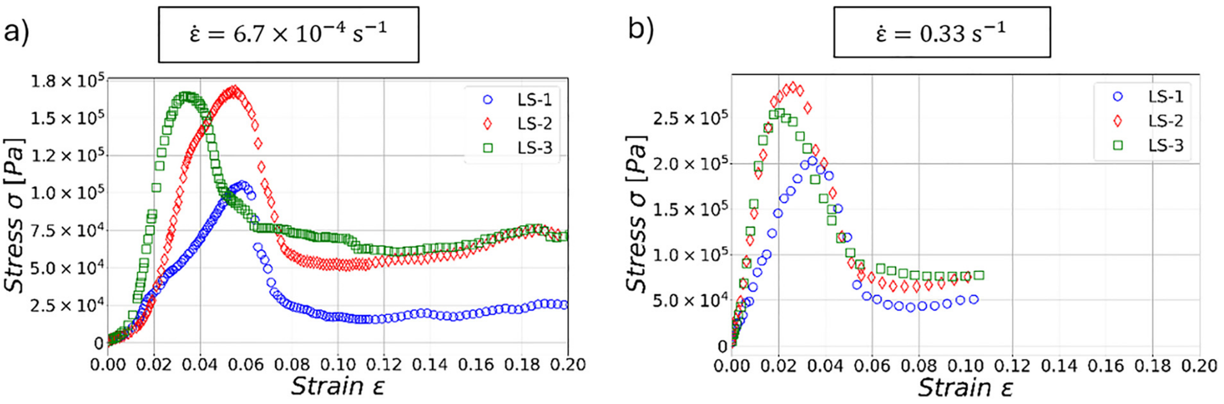

Fig. 14 Stress–strain compression curves of the studied lipsticks LS-1 (blue circles), LS-2 (red diamonds), LS-3 (green squares), obtained at constant displacement rates of $\dot{\varepsilon} = 6.7 \times 10^{-4}$ s$^{-1}$ (a) and $\dot{\varepsilon} = 0.33$ s$^{-1}$ (b).

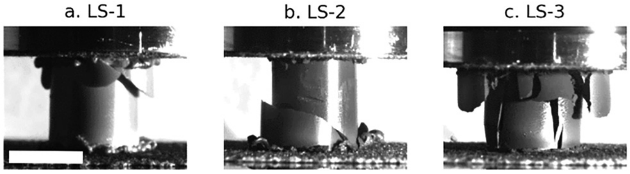

Fig. 15 Post-mortem fracture facies of lipstick samples following uniaxial compression tests shown in Fig. 14a. ~45° cracks are visible for LS-1 (a) and LS-2 (b). Vertical cracks are observed for LS-3 (c). The length of the white scale is 10 mm.

and viscous components. At large displacement rates, the elastic component is dominant while at lower displacement rates, the viscous component becomes more pronounced. This time-dependent nature was investigated in detail in the oscillatory rheology section presented above.

# Discussion

### Construction and limitations of the rheological model

Creep modeling using simple rheological elements like springs, dashpots or friction pads has not yet been explored in the context of lipsticks or comparable makeup materials. To evaluate possible approaches, we considered viscoelastic systems with multiphase 3D networks, such as waxy crude oils and soils. Dey and Basudhar reviewed rheological models for viscoelastic soils, including Maxwell, Kelvin-Voigt, and Burgers models, and concluded that while simple models are convenient, they often fail to capture the full time-dependent behavior.[64] Similarly, Sun *et al.* developed a model for waxy crude oil gels combining one Maxwell and two Kelvin-Voigt elements, noting that a simple Burgers model with a single Kelvin-Voigt element was insufficient to capture the initial response.[65] Following this reasoning, we found that even two Kelvin-Voigt elements could not account for the continuous relaxation spectrum of lipsticks. This motivated our use of a KWW-based creep model, which provides a continuous distribution of relaxation times and allows estimation of the spectrum width and viscoelastic parameters.

Moreover, our results revealed significant nonlinearities in the behavior of lipsticks as they approach structural collapse. Our model is limited to describing only the linear behavior of lipsticks and would need to be more complex to account for nonlinearities. Dey and Basudhar suggest addressing this by incorporating nonlinear springs and dashpots into the model, replacing the linear mechanical elements.[64] An additional Bingham body with a loading criterion can also be included to effectively model plastic nonlinearities before collapse.[49] Other studies on rheological modeling mention the use of the Abel element to account for complex rheological behaviors, such as time-dependency and nonlinear responses.[66,67] Finally, fractional viscoelastic models offer a promising approach that can accurately capture the time-dependent, nonlinear behavior of materials, using fewer parameters. They have proven to be particularly relevant for oleogel systems.[68]

### Understanding lipstick structural breakdown mechanisms through LAOS analysis

LAOS analysis provides valuable insights into the material behavior during structural breakdown.[46,69,70] While very few studies were published so far on the LAOS analysis of commercial lipsticks at room temperature, our findings are in agreement with those from Pan and Germann, showing similar L–B curve shapes and consistent $S$ and $T$ ratio evolution, illustrating intracycle shear-thinning and strain-stiffening in lipsticks at lip temperature (32 °C).[11] Strain-stiffening is characterized by an increase in material stiffness at large strains and may result from percolation between crystals in the three-dimensional network.[71] Shear-thinning is marked by a decrease in viscosity at high shear rates, which is desirable in conditions of use, as the material needs to be easily spreadable during application on the lips.[42] These non-linear behaviors were also observed in other wax-oil materials such as waxy crude oils and candelilla oleogels.[72,73] Intracycle strain-stiffening is common in various viscoelastic materials, including gelatin, cellulose hydrogels, and processed cheese spreads,[46,74,75] while shear-thinning is observed in cosmetic creams and skincare products as it contributes to achieving the desirable textures for customers.[76,77] Thus, it is consistent to observe similar non-linear properties in our reference lipsticks. Strain-stiffening and shear-thinning behaviors were also identified for polymeric systems.[70,82]

The quantitative data shows that the harder material LS-3 exhibits a greater intracycle viscous contribution to non-linearity, whereas the softer one LS-1 shows a higher intracycle elastic contribution (Fig. 11). This difference may be attributed to the larger ductility of LS-1, which allows for structural rearrangements within its three-dimensional network. In contrast, LS-3 is less prone to stress relaxation through plastic deformation and relies on its viscous properties for stress relaxation. These hypotheses are consistent with the additional quantitative results obtained from FT-rheology and displayed in Fig. 10, which revealed a distinct nonlinear response in LS-3 compared to the other lipsticks. This difference may be attributed to the more brittle nature of LS-3, which could result in less efficient stress relaxation in inelastic deformation. Similar findings have been reported by Macias–Rodriguez in a comparative study of laminating and all-purpose shortenings (fats used for baking).[39] This interpretation is further supported by the compression experiments, which highlighted the more brittle nature of LS-3 compared to the other grades, with a higher propensity for crack propagation (Fig. 14 and 15). Furthermore, the FT-analysis revealed a sharp increase in the third harmonic magnitude for the soft material LS-1, followed by a significant decrease as strain amplitude increases. This trend suggests that after an initial strong nonlinear response, the material reaches a more stable state, likely associated with a structural rearrangement, such as a phase alignment under shear strain.[44,78]

### Evidence supporting an intertwined crystalline-polymeric network in lipstick structure

Our experimental observations revealed a distinctive rheological signature indicative of a system based on structural elements and governed by a continuous spectrum of relaxation times. Considering the composition of the lipsticks, which mainly include waxes and polymers as structuring agents, as well as the thermal sweeps revealing an elastic residue beyond the melting point, a possible interpretation lies in the presence of an intertwined crystalline-polymeric network in the lipstick microstructure. This hybrid network would consist of percolated wax crystals and entangled polymer chains, embedded in high viscosity oils and polymer-swollen oil phases, with networks interacting closely to govern the overall rheological response of the material.

This interpretation is further supported by the frequency-dependent rheological behavior, which is consistent with a polymer–wax structure in which polymers are embedded within the crystalline wax framework. Their constrained mobility gives rise to a broad relaxation spectrum, resulting in a predominantly elastic response at higher frequencies, while the response becomes more viscous at smaller frequencies.

Indeed, it is known that the elastic stiffness in a polymer network is entropic in origin, as deformation reduces the freedom of mobility of the polymer chains.[79,80] This means that the network becomes stiffer when the polymer chains are stretched, due to a reduction in thermal fluctuations. Our oscillatory rheology measurements revealed a cutoff frequency around 0.1 Hz. This observation thus provides support for the proposed mechanism: above the cutoff frequency of 0.1 Hz, the polymer network has no time to relax, and thermal fluctuations are effectively suppressed, leading to a straightening of the chains. As a result, the elastic stiffness of the network increases and the elastic contribution to the stress response becomes largely dominant, resulting in a smaller damping factor. In this large-frequency regime, the rheological response reflects contributions from both the stretched polymer chain network and the stiff wax crystals network. However, at frequencies below the 0.1 Hz cutoff, we observe an increase in the damping factor. This reflects a decrease in the elastic stiffness of the polymer network. At these small frequencies, the network has sufficient time to relax: the chains can slide past each other, and slow inelastic rearrangements become the primary dissipation mechanism, resulting in enhanced viscous dissipation.[81] Thus, the characteristic cutoff frequency likely marks the onset of thermal fluctuations suppression in the polymer network. Although our measurements do not extend below 0.01 Hz, the shape of the curves suggests that a crossover of the viscoelastic moduli would occur slightly below 0.01 Hz if the curves were extended further. This crossover, associated with the KWW characteristic relaxation time $\tau$, is likely induced by the relaxation of the wax crystal network at smaller frequencies, marking the onset of the terminal flow regime.

Moreover, the coexistence of intracycle strain-stiffening and shear-thinning nonlinearities is associated with the structural networks in presence, identified through the LAOS experiments. On the one hand, intracycle strain-stiffening, reflecting the elastic contribution, is likely arising from the percolation of the wax crystal network as well as the stretching of polymer chains under increasing strain, leading to enhanced stiffness. On the other hand, the intracycle shear-thinning behavior, associated with the viscous contribution, may arise from the alignment of wax crystals and increased mobility of entangled polymer chains, beginning to slide more freely as the strain rate increases.[85]

The KWW stretched-exponential creep model provides a comprehensive framework for describing the rheological behavior of lipsticks, as it accounts for a continuous spectrum of relaxation. This model is consistent with the interpretation of the material as an intertwined network of wax crystals and embedded polymer chains. In such a network, different structural elements relax over different timescales: polymer chains respond at short times, while larger wax domains and their interaction contribute to long-time relaxation. Moreover, the distribution of characteristic lengths, from polymer segments to crystal aggregates, produces a wide relaxation spectrum captured by the KWW model through a characteristic relaxation time $\tau$ and stretching exponent $\beta < 1$. In other material classes, the KWW exponent has been linked to underlying structural heterogeneity. In glass science, $\beta$ has been related to material fragility, which reflects how rapidly the relaxation time increases near the glass transition: more fragile glasses exhibit a broader distribution of relaxation times (lower $\beta$), while stronger glasses show more uniform dynamics (higher $\beta$).[83] Similarly, in PMMA polymer networks, the $\beta$ exponent has been associated with variations in cross-linking density.[84] These interpretations suggest that $\beta$ may similarly reflect the degree of structural heterogeneity in lipstick formulations.

## Linking mechanical parameters to use properties of lipsticks

Rheological measurements revealed that all reference lipsticks follow a typical viscoelastic behavior, with significant elastic contribution in the linear zone and complex nonlinear

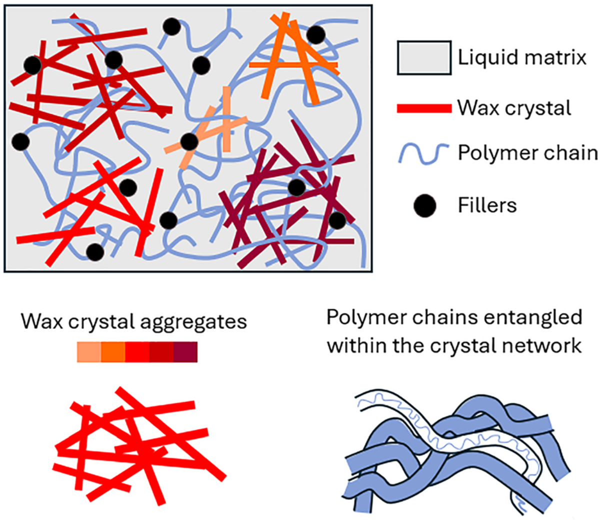

Fig. 16 Schematic representation of the structure of lipsticks, illustrating its intertwined crystalline-polymeric network architecture embedded in a polymer-swollen and high viscosity oils liquid phase. The wax color gradient represents the size of the crystal aggregates, with darker colors corresponding to larger aggregates.

behavior. Analyzing both shear rheological and compression properties provided valuable insights into the application characteristics of lipsticks.

Our results suggest an intertwined structure consisting of a softer, yet tough, network of entangled polymer chains embedded in a stiff wax crystal network (Fig. 16). The synergy between these two components likely contributes to the mechanical stability of the material, producing a structure with high rigidity and ductility. In the specific case of lipsticks, the stiff network formed through the physical percolation of wax crystals provides elasticity and strength to the stick, enabling it to withstand mechanical loads during application on lips. Meanwhile, the softer polymer network provides ductility, allowing the material to deform without catastrophic failure and enhancing deposition on the lips thanks to the weak bonds linking the polymer chains. During the fracture of the material, we expect that the brittle wax crystal network dissipates energy through internal bond breakage.[26] Simultaneously, sliding entanglements of polymer chains form an oriented structure under strain, enhancing toughness and slowing down crack propagation.[86]

## Conclusion

This study provides a comprehensive investigation of the structure and rheology of three commercially available lipsticks through an experimental approach. Given the limited data in the literature on the mechanical behavior of commercial lipsticks, exploring their fundamental mechanical properties enhanced our understanding of their responses to axial and shear solicitations.

Oscillatory rheological amplitude sweeps indicate a linear viscoelastic zone for $\gamma < 10^{-3}$, with distinct nonlinearities emerging from $\gamma \approx 10^{-2}$. LAOS rheology measures offered valuable insights into the structural breakdown of the materials under shear strain, highlighting nonlinear phenomena such as intracycle strain-stiffening and shear-thinning. Our results indicate that while all three lipsticks exhibit a broadly similar behavior in the linear regime, with varying rigidity and damping values, they differ primarily in their stress relaxation mechanisms under loading. We propose a KWW-based model as a creep rheological model for lipsticks, as it appears suitable for all tested lipsticks when comparing to our experimental data and enables material parameter estimation as well as linear behavior prediction. The KWW model brings out a continuous spectrum of relaxation times characterized by the stretching exponent $\beta$, which reflects the heterogeneous and complex nature of the lipstick structure. By integrating our observations with results from various testing methods, we identified a distinct rheological signature which might be linked to the presence of an intertwined crystalline-polymeric network architecture likely underlying the mechanical integrity of lipsticks. To complete this study, further research should focus on the mechanisms leading to material failure by conducting an in-depth investigation into crack propagation. Moreover, understanding the mechanisms by which different formulae affect lipstick mechanical properties would enhance the formulation research process in the cosmetics industry.

## Author contributions

M. Gautier: conceptualization, resources, data curation, investigation, visualization, writing – original draft, writing – review & editing. T. To: conceptualization, investigation, writing – review & editing. A.-S. Botte: conceptualization, investigation. J. Dupire: conceptualization, supervision, funding acquisition and project administration, writing – review & editing. T. Rouxel: conceptualization, supervision, funding acquisition and project administration, writing – review & editing. F. Artzner: conceptualization, supervision, funding acquisition and project administration, writing – review & editing.

## Conflicts of interest

There are no conflicts to declare.

## Data availability

Detailed LAOS rheology methodology; additional figures on the microstructure/rheological properties relationships and Fourier-Transform rheology; comparison of different rheological models; and raw data corresponding to the figures presented in the article are included in the supplementary information (SI). See DOI: https://doi.org/10.1039/d5sm01032b.

## Acknowledgements

We are indebted to Thierry Aubry (Univ. Bretagne Ouest) for fruitful discussions and advice regarding the rheological analysis and modeling, and we thank Pascal Panizza (Univ. PSL) for valuable support with the rheology experiments. The authors would like to thank the anonymous referees for their valuable suggestions, which helped improve the quality of the manuscript.

## References

1 M. Ogilvie and P. Kristensen-Bach Edith, ECU Publications, 2001, In proceedings of the 2001 ANZMAC: Bridging Market.
2 N. Etcoff, *Survival of the prettiest: The science of beauty*, Anchor Books, Doubleday, New York, NY, US, 1999.
3 N. Eskandari, E. De Carlo, F. Zorzi, S. Dall'Acqua, C. Furlan, G. Artioli and M. Vidale, *Sci. Rep.*, 2024, **14**, 1–7.
4 H. De Clermont-Gallerande, S. Abidh, A. Lauer, S. Navarro, G. Cuvelier and J. Delarue, *OCL: Oilseeds Fats, Crops Lipids*, 2018, **25**, 3–13.
5 D. MacDonald and Y. Dildar, *J. Behav. Exp. Econ.*, 2020, **86**, 101527.

6 S. E. Hill, C. D. Rodeheffer, V. Griskevicius, K. Durante and A. E. White, *J. Abnorm. Soc. Psychol.*, 2012, **103**, 275–291.

7 H. De Clermont-Gallerande, *OCL: Ol., Corps Gras, Lipides*, 2006, **13**, 322–325.

8 H. De Clermont-Gallerande, C. Daquin, C. Malvezin, C. Lesbros, C. Nagahiro, E. Bertron, N. Slaim, M. A. Sanchez, O. Pichoutou and P. Guarillof, *OCL: Ol., Corps Gras, Lipides*, 2022, **29**, 1–16.

9 N. Rasheed, S. A. Rahman and S. Hafsa, *Res. J. Pharm. Technol.*, 2020, **13**, 1693–1700.

10 L. Budai, I. Antal, I. Klebovich and M. Budai, *J. Cosmet. Sci.*, 2012, **63**, 93–101.

11 S. Pan and N. Germann, *Acta Mech.*, 2020, **231**, 3031–3042.

12 M. S. Shimizu, Y. Nomura and H. S. Bui, *Surface Science and Adhesion in Cosmetics*, John Wiley & Sons, 2021, pp. 35–72.

13 P. Snabre and D. Habouzit, *CFM 2013-21ème Congrès Français de la Mécanique*, AFM, Maison de la Mécanique, Courbevoie, 2013, pp. 1–6.

14 S. Y. Seo, I. S. Lee, H. Y. Shin, K. Y. Choi, S. H. Kang and H. J. Ahn, *Int. J. Cosmet. Sci.*, 1999, **21**, 207–216.

15 A. Kermarec, *PhD thesis*, Université Bordeaux 1, France, 2011.

16 H. Wang, S. A. E. Boyer, M. Bellet and F. Dalle, *Cryst. Growth Des.*, 2023, **23**, 1422–1433.

17 A. I. Blake and A. G. Marangoni, *Food Biophys.*, 2015, **10**, 456–465.

18 P. Thareja, *Rheol. Acta*, 2013, **52**, 515–527.

19 H. Hwang, S. Kim, K. O. Evans, C. Koga and Y. Lee, *Food Struct.*, 2015, **5**, 10–20.

20 T. Imai, K. Nakamura and M. Shibata, *Colloids Surf., A*, 2001, **194**, 233–237.

21 A. G. Marangoni and S. S. Narine, *Food Res. Int.*, 2002, **35**, 957–969.

22 T. H. Shellhammer, T. R. Rumsey and J. M. Krochta, *J. Food Eng.*, 1997, **33**, 305–320.

23 R. G. Drew, *J. Soc. Cosmet. Chem.*, 1978, **29**, 441–446.

24 T. Mitsui, K. Morosawa and C. Ōtake, *J. Texture Stud.*, 1971, **2**, 339–347.

25 J. P. Gong, Y. Katsuyama, T. Kurokawa and Y. Osada, *Adv. Mater.*, 2003, **15**, 1155–1158.

26 S. B. Walker and S. M. Fielding, *Phys. Rev. Lett.*, 2025, **135**, 188201.

27 A. A. Moud, M. Kamkar, A. Sanati-Nezhad, S. H. Hejazi and U. Sundararaj, *Colloids Surf., A*, 2021, **609**, 125577.

28 Z. Zhang, L. Sun, X. Liu and X. Huo, *Colloids Surf., A*, 2023, **678**, 132445.

29 J. Yang, K. Li, C. Tang, Z. Liu, J. Fan, G. Qin, W. Cui, L. Zhu and Q. Chen, *Adv. Funct. Mater.*, 2022, **32**, 2110244.

30 Z. Gu, K. Huang, Y. Luo, L. Zhang, T. Kuang, Z. Chen and G. Liao, *Wiley Interdiscip. Rev.: Nanomed. Nanobiotechnol.*, 2018, **10**, 1–15.

31 I. Tavernier, C. D. Doan, D. Van De Walle, S. Danthine, T. Rimaux and K. Dewettinck, *RSC Adv.*, 2017, **7**, 12113–12125.

32 P. G. De Gennes, *J. Chem. Phys.*, 1971, **55**, 572–579.

33 H. S. Ashbaugh, A. Radulescu, R. K. Prud, D. Schwahn, D. Richter and L. J. Fetters, *Macromolecules*, 2002, **35**, 7044–7053.

34 A. Silberman, E. Raninson, I. Dolgopolsky and S. Kenig, *Polym. Adv. Technol.*, 1995, **6**, 643–652.

35 S. B. Mehta, M. Shribak and R. Oldenbourg, *J. Opt.*, 2013, **15**, 094007.

36 M. Robin, C. Djediat, A. Bardouil, N. Baccile, C. Chareyron, I. Zizak, P. Fratzl, M. Selmane, B. Haye, I. Genois, J. M. Krafft, G. Costentin, T. Azaïs, F. Artzner, M. M. Giraud-Guille, P. Zaslansky and N. Nassif, *Adv. Sci.*, 2024, **11**, 1–14.

37 C. A. Schneider, W. S. Rasband and K. W. Eliceiri, *Nat. Methods*, 2012, **9**, 671–675.

38 B. A. Macias-Rodriguez and A. A. Marangoni, *Crit. Rev. Food Sci. Nutr.*, 2018, **58**, 2398–2415.

39 B. A. Macias-Rodriguez, *Structure-Function Analysis of Edible Fats*, Elsevier Inc., 2019, pp. 169–195.

40 K. Hyun, M. Wilhelm, C. O. Klein, K. S. Cho, J. G. Nam, K. H. Ahn, S. J. Lee, R. H. Ewoldt and G. H. McKinley, *Prog. Polym. Sci.*, 2011, **36**, 1697–1753.

41 R. H. Ewoldt, G. H. McKinley and A. E. Hosoi, *J. Rheol.*, 2008, **52**, 1427–1458.

42 S. Pan and N. Germann, *Thermochim. Acta*, 2019, **679**, 178332.

43 B. A. Macias-Rodriguez and A. G. Marangoni, *Rheol. Acta*, 2016, **55**, 767–779.

44 M. Wilhelm, *Macromol. Mater. Eng.*, 2002, **287**, 83–105.

45 R. H. Ewoldt, *J. Rheol.*, 2013, **57**, 177–195.

46 A. M. Le, M. Y. Erturk and J. Kokini, *J. Food Eng.*, 2023, **336**, 111193.

47 M. Y. Erturk, S. A. Rogers and J. Kokini, *Food Hydrocolloids*, 2022, **128**, 107558.

48 M. Dogan, A. Kayacier, Ö. S. Toker, M. T. Yilmaz and S. Karaman, *Food Bioproc. Technol.*, 2013, **6**, 1420–1433.

49 S. Wang, J. Qi, Z. Yin, J. Zhang and W. Ma, *Cold Reg. Sci. Technol.*, 2014, **107**, 47–54.

50 D.-L. Chen, P.-F. Yang and Y.-S. Lai, *Microelectron. Reliab.*, 2011, **52**, 541–558.

51 N. Saboo and A. Mudgal, *Pet. Sci. Technol.*, 2018, **36**, 1627–1634.

52 F. L. Cumbrera, F. Sanchez-Bajo, F. Guiberteau, J. D. Solier and A. Muñoz, *J. Mater. Sci.*, 1993, **28**, 5387–5396.

53 A. R. Patel, M. Babaahmadi, A. Lesaffer and K. Dewettinck, *J. Agric. Food Chem.*, 2015, **63**, 4862–4869.

54 R. Campos, S. S. Narine and A. G. Marangoni, *Food Res. Int.*, 2002, **35**, 971–981.

55 Y. Yao, H. Zhou, W. Liu, C. Li and S. Wang, *J. Oleo Sci.*, 2021, **70**, 135–143.

56 H. S. Lee, P. Singh, W. H. Thomason and H. S. Fogler, *Energy Fuels*, 2008, **22**, 480–487.

57 A. L. Silva and A. P. Coutinho, *Rheol. Acta*, 2004, **43**, 433–441.

58 J. Cesar, B. Rocha, J. Dutra, M. Cristina, N. Mascarenhas, D. Barrera, L. Maria, R. Guerreiro and R. Lopes, *Food Res. Int.*, 2013, **50**, 318–323.

59 T. S. K. Ng and G. H. McKinley, *J. Rheol.*, 2008, **52**, 417–449.

60 T. G. Mason, J. Bibette and D. A. Weitz, *Phys. Rev. Lett.*, 1995, **75**, 2051–2054.

61 A. H. W. Ngan, H. T. Wang, B. Tang and K. Y. Sze, *Int. J. Solids Struct.*, 2005, **42**, 1831–1846.

62 T. Chudoba and F. Richter, *Surf. Coat. Technol.*, 2001, **148**, 191–198.

63 G. Feng and A. H. W. Ngan, *MRS Proc.*, 2000, **649**, Q7.1.

64 A. Dey and P. K. Basudhar, *GeoFlorida 2010: Advances in Analysis, Modeling & Design*, 2010, pp. 2611–2620.

65 G. Sun, J. Zhang and H. Li, *Energy Fuels*, 2014, **28**, 3718–3729.

66 H. Zhou, T. Su, H. Deng, R. Wang, J. Zhao, X. Sun and L. An, *Mech. Time Depend Mater.*, 2021, **25**, 85–100.

67 Z. Zhang, L. Hou, X. Chen, Y. Zhou, M. Liu and W. Zhou, *J. Dispersion Sci. Technol.*, 2016, **37**, 326–332.

68 A. Bonfanti, J. Kaplan, G. Charras and A. Kabla, *Soft Matter*, 2020, **16**, 6002–6020.

69 L. Guo, X. Han, Y. Lei, L. Wang and P. Yu, *J. Pet. Sci. Eng.*, 2022, **213**, 110444.

70 C. Daniel, I. W. Hamley, M. Wilhelm and W. Mingvanish, *Rheol. Acta*, 2001, **40**, 39–48.

71 C. Jiang and S. G. Srinivasan, *Nature*, 2013, **496**, 339–342.

72 E. R. Werner-Cárcamo, Y. Soleimaniam, B. A. Macias-Rodriguez, M. Rubilar and A. G. Marangoni, *Food Res. Int.*, 2024, **189**, 114579.

73 C. Dimitriou, *PhD thesis*, Massachusetts Institute of Technology, USA, 2010.

74 W. Sun, L. Huang, Y. Yang, X. Liu and Z. Tong, *Chin. J. Polym. Sci.*, 2015, **33**, 70–83.

75 Q. Meng and Y. Gao, *Int. J. Solids Struct.*, 2023, **276**, 112325.

76 I. Kaneda, in *Rheology of Biological Soft Matter*, ed. I. Kaneda, Springer Japan, Tokyo, Japan, 2017, pp. 295–321.

77 F. Cyriac, T. X. Yi and P. S. Chow, *Biotribology*, 2023, **35–36**, 100249.

78 Y. Séréro, V. Jacobsen, J. F. Berret and R. May, *Macromolecules*, 2000, **33**, 1841–1847.

79 M. Langela, U. Wiesner, H. W. Spiess and M. Wilhelm, *Macromolecules*, 2002, **35**, 3198–3204.

80 M. L. Gardel, J. H. Shin, F. C. MacKintosh, L. Mahadevan, P. Matsudaira and D. A. Weitz, *Science*, 2004, **304**, 1301–1305.

81 J.-C. Milstein Joshua and N. Meiners, in *Encyclopedia of Biophysics*, ed. G. C. K. Roberts, Springer Berlin Heidelberg, Berlin, Heidelberg, 2013, pp. 2757–2760.

82 L. Deng, X. Trepat, J. P. Butler, E. Millet, K. G. Morgan, D. A. Weitz and J. J. Fredberg, *Nat. Mater.*, 2006, **5**, 636–640.

83 R. Böhmer, K. L. Ngai, C. A. Angell and D. J. Plazek, *J. Chem. Phys.*, 1993, **99**, 4201–4209.

84 N. M. Alyes, J. L. Gómez Ribelles, J. A. Gómez Tejedor and J. F. Mano, *Macromolecules*, 2004, **37**, 3735–3744.

85 G. J. Donley, M. Bantawa and E. Del Gado, *J. Rheol.*, 2022, **66**, 1287–1304.

86 T. Nakajima, T. Kurokawa, S. Ahmed, W. L. Wu and J. P. Gong, *Soft Matter*, 2013, **9**, 1955–1966.